Journal of
Materials Chemistry A
Materials for energy and sustainability

This article can be cited before page numbers have been issued, to do this please use: S. Rezakhani, H. Shahroosvand, P. Gao and M. K. Nazeeruddin, *J. Mater. Chem. A*, 2025, DOI: 10.1039/D5TA02440D.

ROYAL SOCIETY
OF CHEMISTRY

rsc.li/materials-a

View Article Online
DOI: 10.1039/D5TA02440D

Innovating Carbon-Based Perovskite Solar Cells: The Role of a CN-Anchoring Self-Assembled Molecular Layer in Efficiency and Stability

Sheida Rezakhani,[a] Hashem Shahroosvand,[a*] Peng Gao,[b] Mohammad Khaja Nazeeruddin[c*]

[a] Sh. Rezakhani, Prof. H. Shahroosvand
Group for Molecular Engineering of Advanced Functional Materials (GMA), Chemistry Department, University of Zanjan, Zanjan, Iran
E-mail: shahroos@znu.ac.ir

[b] Prof. P. Gao
Laboratory for Advanced Functional Materials, Xiamen Institute of Rare Earth Materials, Haixi Institute, Chinese Academy of Sciences, Xiamen 361021, China
E-mail: p_gao@foxmail.com

[c] Prof. M. Khaja Nazeeruddin
Group for Molecular Engineering of Functional Materials, Institute of chemical Sciences and Engineering, École Polytechnique Fédérale de Lausanne, CH-1951 Sion, Switzerland
E-mail: mdkhaja.nazeeruddin@epfl.ch

[d]School of Integrated Circuits, Southeast University, Wuxi, Jiangsu, 214026 P. R. China

Abstract

The discovery of self-assembled molecular layer (SAML) containing anchoring groups such as COOH and PO3H as efficient hole-selective materials (HSMs) in p-i-n perovskite solar cells (PSCs) is pivotal for enhancing the interaction between HSMs and perovskite layers. In this work, we propose, for the first time, The HSM featuring CN groups as anchoring groups in n-i-p devices, achieving a power conversion efficiency (PCE) of 20.37% using a carbon electrode. The HSM is based on a phenanthroimidazole backbone linked to Aza and cyanide groups. VASP computational studies reveal that the new HSM can coordinate to Pb atoms in the perovskite layer through CN groups in a bridging mode (where two CN groups bond to two Pb atoms), with an adsorption energy (E_{ads}) of -1.04 eV. These SAMLs demonstrate greater stability compared to the classic spiro-OMeTAD, with a remarkable one-year operational stability. The photo- and thermal-stability of PSCs incorporating the new SAMLs are notable, retaining approximately 97.5% of their initial PCE after 600 hours at 80 ºC under ambient

View Article Online
DOI: 10.1039/D5TA02440D

conditions. Additionally, the devices have exhibited impressive visual stability for over one year. The operational stability of carbon electrodes PSCs, combined with the versatility of CN-functionalized organic molecules, positions these materials as promising candidates for the large-scale production of PSCs with metal-free electrodes, eliminating the need for thermal evaporation techniques. Our findings represent a paradigm shift from conventional spiro-OMeTAD-based hole transporting materials to novel SAML-based HSMs, paving the way for advancements in PSC technology

1. Introduction

Hole transport material (HTM) in perovskite solar cells (PSCs) plays a key role in achieving high power conversion efficiencies (PCE) by reducing recombination at the interface between the perovskite and the contact layer. A variety of HTMs - ranging from small molecules to polymers and p-type inorganic semiconductors - have been extensively investigated in PSCs [1-3]. Recent advancements in the field have highlighted the potential of anchoring groups containing self-assembled molecular layer (SAML) materials as efficient hole-selective materials (HSMs). As an interface engineering strategy, SAMLs can effectively serve as HSMs to replace the conventional HTM in PSCs, leveraging their structural advantages to optimize device efficiency [4-7]. We abandoned the term of ’self-assembled monolayer’, because they are proven to be not a monolayer. SAML HSMs promote smooth morphology and improved crystallinity of the perovskite film by adsorbing spontaneously onto the substrate surface, thereby enhancing device performance [8]. Moreover, SAMLs modulate the surface dipole moment, impacting charge transfer and recombination dynamics. They facilitate homogeneous perovskite layer formation, resulting in improved fill factor (FF) and open-circuit voltage (V_{OC}) [9, 10]. SAMLs also boast advantages such as solubility in environmentally friendly solvents,

View Article Online
DOI: 10.1039/D5TA02440D

reduced biotoxicity, minimal material consumption, straightforward fabrication processes, and excellent reproducibility [11].

Typically, SAMLs comprise three components: (i) an anchoring group with a strong affinity for the substrate; (ii) a linker group that facilitates molecular ordering through noncovalent interactions; and (iii) a terminal group responsible for charge transport [12, 13]. The selection of the anchoring group is critical, as it influences binding energy, surface dipole moment, charge transfer, and recombination in the device. Common anchoring groups include phosphonic acid (PA), carboxylic acid (CA), cyanoacetic acid (CAA), and cyanoacrylic acid [14, 15].

Pb^{2+} cations related deep-level defects in the perovskite layer significantly contributes to the non-radiative recombination, hampering charge transfer and promotes photochemical degradation at the interface [16]. To mitigate these issues, it is essential to employ compounds that reduce such defect densities. Cyano groups are known to acts as a Lewis base, forming coordination bonds with Pb^{2+} ions on the perovskite surface, enhancing performance [17, 18]. Several cyano-containing HTMs with commendable efficiencies have been reported, as summarized in the Supplementary Information (SI).

Among organic photovoltaic materials, azo dyes are particularly notable and have been utilized in dye-sensitized, organic, and perovskite solar cells [19]. Derivatives of azo compounds that exhibit donor-π-acceptor (D-π-A) structures display excellent photovoltaic properties due to their extensive π-delocalized systems, where minor modifications in donor or acceptor groups can significantly impact photo-physical and photochemical characteristics [20, 21].

In this study, we synthesized a new diazo compound, diCNq-Aza, with a D-π-A structure as a SAML-type HSM (SAML-HSM) and investigated its application in PSCs. The synthetic pathway for producing this compound is straightforward, requiring no expensive purification techniques or costly organometallic catalysts, leading to significant cost reductions. Notably, this HSM does not necessitate chemical oxidation or the incorporation of doping agents such as LITFSI and t-butyl pyridine to achieve high PCEs, making it a promising alternative for use

View Article Online
DOI: 10.1039/D5TA02440D

in n-i-p type PSCs. We employed a combination of theoretical and experimental approaches to investigate the electronic properties of the new HSM and to understand the electron distribution within the designed structure. The CN group as the anchoring moiety bond to two Pb atoms in a bridging mode, which enhances charge transfer and effectively passivates the perovskite. The PCE of the PSC using the carbon electrode surpassed that of spiro-OMeTAD based devices, achieving approximately 21% PCE, one of the highest reported for carbon-based PSCs. Additionally, the PSC with the new SAML retained over 95% of its initial performance over time - especially at 80 °C - demonstrating exceptional thermal stability. Notably, the PSC showed no signs of decomposition after one year, whereas the fresh perovskite deteriorated within one month. This work paves the way for competitive carbon-based PSCs through the integration of the new CN functionalized SAML-HSM with carbon electrodes.

2. Results and discussion

2.1 Optical, Electrochemical and Thermoanalytical Properties

New SAML-HSM was synthesized by using two sequential pathways to obtain primary compounds 3 and 4, resulting in a C-N coupling to produce diCNq-Aza. In contrast to the routine strategy for preparing C-N coupling by using the Suzuki method based on Pd catalyst, the using of Cs_2CO_3/CuI/1,10-phenanthroline dramatically reduces the total cost of the product. In fact, 1g of catalyst for the synthesis of spiro-OMeTAD is estimated at about 68.5$, while for the new SAML-HSM diCNq-Aza is reduced to 2.53$.

The molecular structure and the synthesis steps of the new SAML diCNq-Aza are illustrated in Figure 1 and explained in more details in the experimental part and SI. New SAML-HSM was fully characterized by spectroscopic methods. ^{1}H-NMR and FTIR spectra of the precursors and the final compound are given in the supplementary (Fig. S1 and Fig. S2).

The interesting molecular structure aspect of the new SAML is the presence of Aza groups, which are linked to diphenyl electron donor moieties, as well CN acceptor groups, which play

View Article Online
DOI: 10.1039/D5TA02440D

as anchoring groups, confirming the D-A structure, which acts as a SAML-HSM. In the following sections, we will first prove the D-A properties of HSM and prove the intraction between CN groups of SAML with Pb atoms in surface of perovskite and then will show which coordination mode of the CN group of new SAML is the favorite to bound perovskite layer by VASP computational studies and finally the calculation of photovoltaic and stability behavior compared to classic spiro-OMeTAD.

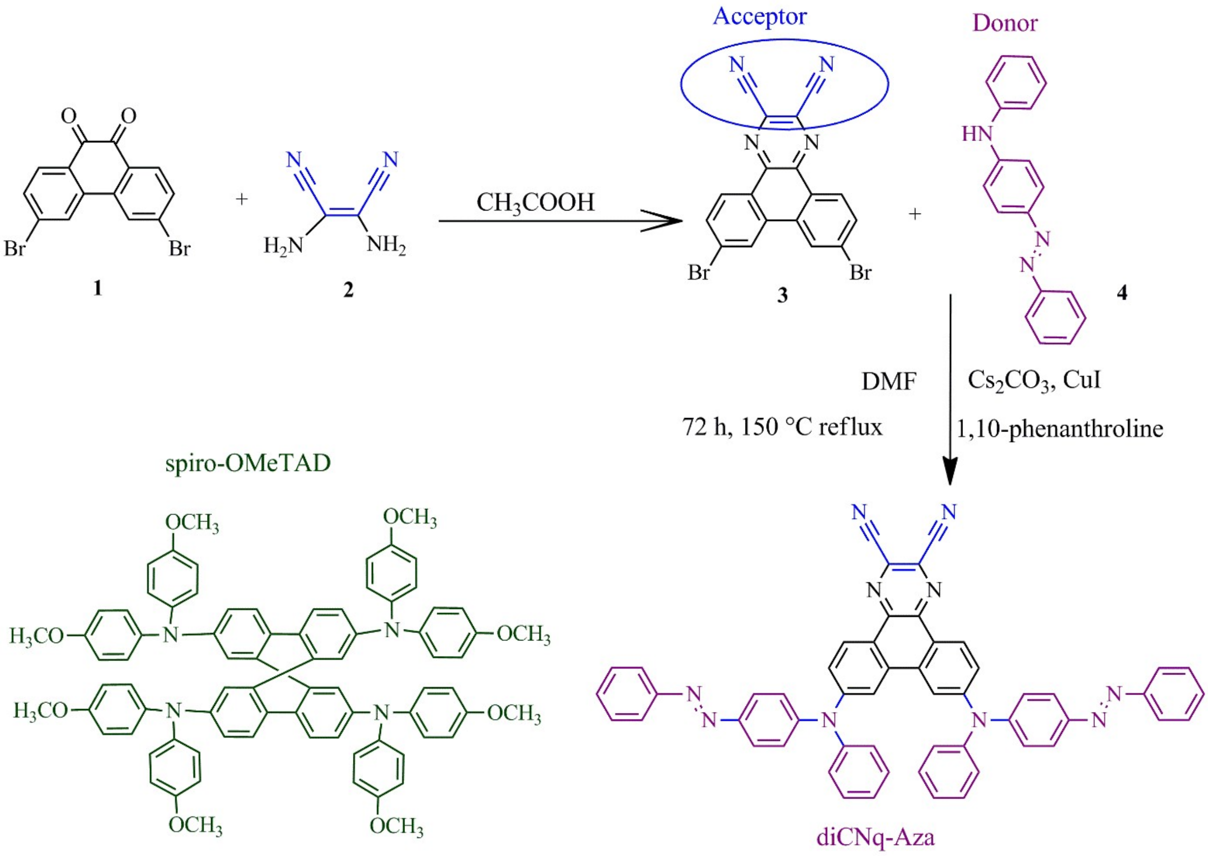

Figure 1. Synthesis reactions and molecular structure. Schematic illustration of the overall reaction mechanism for the formation of diCNq-Aza and spiro-OMeTAD.

To evaluate the band gaps and energy levels of the new SAML-HSM and spiro-OMeTAD molecules, further studies, including optical absorption, light emission, and cyclic voltammetry analysis, were performed. The ultraviolet-visible (UV-Vis) absorption and photoluminescence (PL) emission spectra of diCNq-Aza in acetonitrile are shown in Figure 2a, and the corresponding parameters are listed in Table 1. Two absorption bands are presented at λ_{max} =

296 and 436 nm, and the first one could be attributed to the n-π* transition of aromatic cycles, and the second assigned to the π-π* transitions of the π–electron system [22]. Because the new SAML-HSM showed weak light harvesting in the visible region, therefore, it could not interfere with the light absorption by the perovskite layer [23]. Surprisingly, the wavelength maximum of new SAML-HSM was red-shifted about 48 nm compared to spiro-OMeTAD ones, and the optical band gap (E_g) is 0.57 eV less than spiro-OMeTAD, which means that the intersection wavelength point consequently shifted to higher wavelength.

Furthermore, the PL spectrum of diCNq-Aza displays a maximum emission at $\lambda_{max.\ em}$ = 583 nm, which moved to a higher wavelength of about 160 nm compared to spiro-OMeTAD ($\lambda_{max.\ em}$ = 423 nm), which can be attributed to the presence of strong CN π-acceptor properties as well the extension of π conjugated system. Finally, the intersection wavelength of the UV-Vis and PL spectra of HSM was used to obtain band gap energy values, which are required to calculate the energies of the lowest unoccupied molecular orbitals (E_{LUMO}) for HSM. The obtained E_g for diCNq-Aza is 2.44 eV and has a smaller band gap than spiro-OMeTAD with E_g = 3.01 eV, favoring the thermal population of the conduction band and thus increasing the number of intrinsic charge carriers [24].

Table 1. The optical, electrochemical, thermal and hole mobility data for diCNq-Aza and spiro-OMeTAD

HSM/HTM	$\lambda_{max.abs}$[a] (nm)	$\lambda_{max.em}$[a] (nm)	λ_{int}[b]	E_g[c] (eV)	$E_{1/2}$[d] (eV)	E_{HOMO}[e] (eV)	E_{LUMO}[f] (eV)	T_g (°C)	$\eta_{quench)}$ (%)
diCNq-Aza	296,436	583	508	2.44	0.57	-5.17	-2.73	98.5	95
spiro-OMeTAD	308,388	423	412	3.01	0.57	-5.18	-2.17	124.5	93

[a] UV-Vis and photoluminescence spectra were measured in acetonitrile solution.

[b] λ_{int} is the intersection point of normalized UV–vis absorption and emission curves.

[c] Optical band gap was calculated from the formula $E_g = 1240/\lambda_{int}$.

View Article Online
DOI: 10.1039/D5TA02440D

[d]From CV measurements, $E_{1/2} = 1/2(E_{pa} + E_{pc})$. [e]$E_{HOMO} = -(E_{1/2}$ (vs. Fc/Fc^{+}) +4.8 eV). [f]$E_{LUMO} = E_{HOMO} + E_g$.

Cyclic voltammetry (CV) analysis was carried out to investigate the electrochemical properties of diCNq-Aza and the estimation of energy levels based on the standard equations [25]. As shown in Figure 2b, diCNq-Aza HSM exhibited quasi-reversible oxidation/reduction waves in the positive potential range like the spiro-OMeTAD, which indicates good electrochemical stability in the solution. Comparing the electrochemical data for diCNq-Aza and spiro-OMeTAD**,** it is apparent that the first oxidation half-wave of diCNq-Aza is shifted to a lower potential compared to spiro-OMeTAD. Hence, it is more easily oxidized to diCNq-Aza^{+} than spiro–OMeTAD to spiro–OMeTAD^{+}. The estimated values for the highest occupied molecular orbital energies (E_{HOMO}) of diCNq-Aza and spiro-OMeTAD are -5.17 eV and -5.18 eV, respectively, from the equation $E_{HOMO} = -(E_{1/2}$ (vs. Fc/Fc^{+}) +4.8 eV) where $E_{1/2}$ is obtained from the energy values of the CV spectrum with the following relation: $E_{1/2} = 1/2\ (E_{pc} + E_{pa})$. The HOMO energy of the new HSM is sufficiently more positive than the valence band of the perovskite (-5.5 eV), indicating that the HSM is favorable for effectively extracting holes from the perovskite layer toward the counter electrode. By the relationship of $E_{LUMO} = E_{HOMO} + E_g$, the LUMO energy is obtained, which is equal to -2.73 eV for diCNq-Aza and -2.17 eV for spiro-OMeTAD. Related data are listed in Table 1. Surprisingly, the LUMO energy level of diCNq-Aza is higher than the value of the perovskite conduction band, which is expected to effectively block the undesired electron back-transfer from the perovskite layer to electrode [26].

Here, to achieve more negative formation energy (ΔG) to reach more stability, it is paid more attention to reduce the LUMO energy level through the addition of an electron-withdrawing group (CN). The presence of the CN group in HSM leads to a red shift in the UV-Vis peak and effectively reduces the LUMO energy level and has a significant effect on the performance of PSCs.

On the other hand, the lower LUMO energy enhances the energy alignment between the HSM and the perovskite layer. This improvement facilitates more efficient charge separation, blocks electrons, enhances hole extraction, and reduces recombination losses [27, 28]. Consequently, the new SAML-HSM demonstrates greater electrochemical activity compared to the conventional spiro-OMeTAD, underscoring its suitability as an efficient HSM for PSCs. Furthermore, the ability to absorb light at longer wavelengths extends the absorption spectrum of the perovskite layer, enabling it to harness a broader spectrum of sunlight and potentially increase light-harvesting efficiency [29-33]. Additionally, the T_g of the HSM is a critical parameter for the long-term stability of PSC devices. The Differential Scanning Calorimetry (DSC) curve for diCNq-Aza (Figure 2c) shows a T_g of approximately 95.5 °C, which is comparable to that of spiro-OMeTAD (118.5 °C) [34, 35]. This similarity indicates that diCNq-Aza exhibits good thermal stability, confirming its suitability for use in stable PSCs. In particular, contact angle measurements confirmed that the hydrophobicity properties of the new SAML-HSM are comparable with the best HSM materials reported to date [36, 37]. Measurements were made at t = 0, 3 seconds and 3 minutes from the water drop fall. This result indicates that diCNq-Aza presents a good hydrophobicity with a contact angle > 90^o, which is very close to the angle recorded for spiro-OMeTAD in the t=0 (Figure 2d). Surprisingly, the water contact angle after 3 minutes was not changed and kept its shape in the most stable form on the new SAML-HSM [38]. This means that diCNq-Aza prevents water penetration to the perovskite surface after some minutes and thus does not destroy the perovskite immediately, which is promising for a stable SAML-HSM.

An important and effective factor in increasing the photovoltaic performance and long-term stability of perovskite solar cells is the diminishing of perovskite layer defects. To reduce defects and pin-holes, it is necessary to passivate the perovskite surface. In general, the empty 6p electron orbital of the unsaturated coordination Pb^{2+} ion in perovskite has a strong ability to form coordinate covalent bond with Lewis bases [39]. As a result, the electron-donating atoms in

Lewis base compounds can bind with Pb^{2+} eliminating the defects by deactivating the uncoordinated Pb^{2+} ions[40]. To investigate the molecular interactions between the perovskite layer and the new SAM, FTIR and X-ray photoelectron spectroscopy (XPS) techniques were used. The XPS spectra of the perovskite layers before and after passivation with diCNq-Aza were obtained and are presented in Figure 2. As can be seen, Figure 2e is a high-resolution XPS spectrum of the Pb 4f orbitals, which shows that the binding energies of the two characteristic peaks Pb 4f $_{7/2}$ and Pb 4f $_{5/2}$ have shifted from 138.30 eV and 143.55 eV in the bare perovskite to lower binding energies 137.95 eV and 143.25 eV in the perovskite/diCNq-Aza, respectively. This shift confirms the interaction between the N atom of CN and Pb^{2+} and the formation of a C–N…Pb coordination bond. It is worth noting that two small peaks at 136.50 eV and 141.60 eV appear in the pure perovskite layer, which are related to metallic lead formed as a result of Pb^{2+} reduction. Metallic lead causes surface defects in the perovskite thin film and reduces the efficiency and stability of the PSC. In particular, as shown in the figure 2e, the XPS peaks for metallic lead disappear in the XPS spectra of the perovskite thin films coated with diCNq-Aza. This confirms the coordination of CN with Pb^{2+} and the effective passivation of the defects in the perovskite thin film [41, 42]. Subsequently, as observed in the high-resolution N 1s spectrum, the N 1s peak of the bare film was located at 400.28 eV and shifted to a higher binding energy by 400.89 eV after treatment with the new SAML (Figure 2f). Full survey XPS spectra of perovskite films with and without diCNq-Aza passivation treatment was performed and is presented in the SI section, Figure S1.

Considering that the CN group has a stretching vibration peak at approximately 2200 cm^{-1} in finger print region and as a result of binding to the metal, it shows a red shift due to the reduction of the cyanide bond order, further confirmation of the existence of the interaction between the CN group and Pb^{2+} can be provided by recording and comparing the FTIR spectra of diCNq-Aza before and after placement on the perovskite surface (Figure 2g). The significant wavenumber shift of the CN stretching vibration ($\nu_{C\equiv N}$) of diCNa-Aza to lower values after

View Article Online
DOI: 10.1039/D5TA02440D

placement on perovskite, from 2225 to 2220 cm^{-1} and from 2275 to 2255 cm^{-1} indicates the interaction between Pb^{2+} and the nitrogen atom of the CN group and bond formation. Furthermore, it is worth to note, a peak around to 400-500 cm^{-1} can be attributed to Pb-N bonding which generally reported in literatures [43]. As mentioned in zoomed region of 400-500 cm^{-1}, the highlighted peak at 419 cm^{-1} we attribute to the formation of Pb-N bonding.

View Article Online
DOI: 10.1039/D5TA02440D

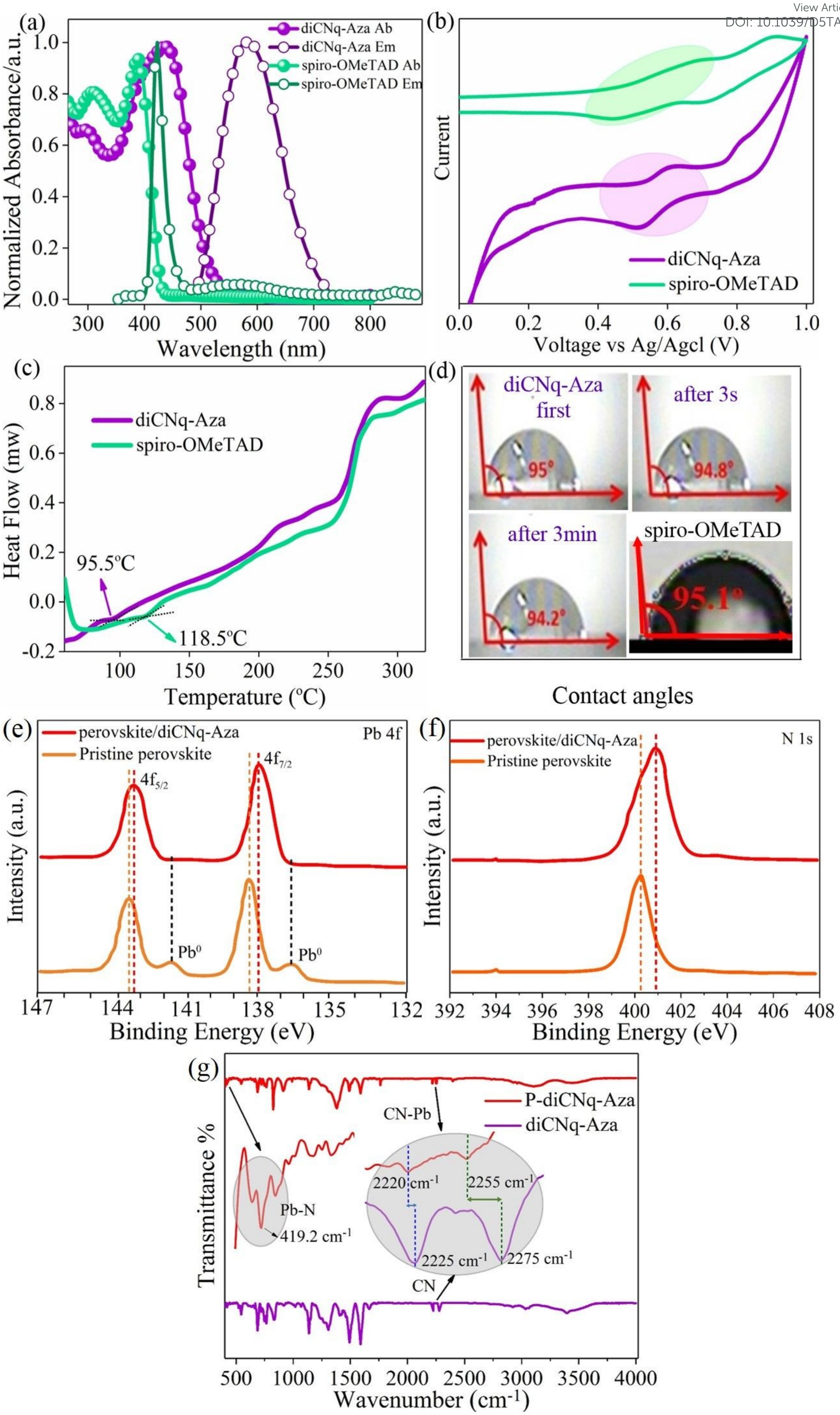

View Article Online
DOI: 10.1039/D5TA02440D

Figure 2. Optical and electrochemical properties of new HSM. **(a)** Normalized absorption (UV-Vis) spectra (left) and luminescence (PL) spectra (right) of diCNq-Aza and spiro-OMeTAD in acetonitrile; **(b)** Cyclic voltammogram (CV) of diCNq-Aza and spiro-OMeTAD in acetonitrile; **(c)** Differential scanning calorimetry (DSC) of diCNq-Aza and spiro-OMeTAD (the value in the image is related to glass transition temperature (T_g)); **(d)** The contact angles of diCNq-Aza and spiro-OMeTAD; **(e)** Pb 4f XPS spectra of perovskite films with and without diCNq-Aza passivation treatment; **(f)** N 1s XPS spectra of perovskite films with and without diCNq-Aza passivation treatment; **(g)** FTIR spectra of diCNq-Aza and p/diCNq-Aza films.

2.2 Hole mobility and SAML characteristics

A schematic structure and layer arrangement of a carbon-based perovskite solar cell (C-PSC) using diCNq-Aza as a new SAML-HSM is shown in Figure 3a. Moreover, the energy-level diagram of diCNq-Aza in Figure 3b shows that the estimated HOMO level of diCNq-Aza optimally matches with the valance band of the perovskite. In particular, the energy difference between the HOMO levels of the perovskite and diCNq-Aza ($\Delta HOMO_{perovskite\text{-}diCNq\text{-}Aza}$) is 0.33 eV, which produces the driving force necessary to hole transfer from perovskite to HSM, confirming the better consistency between the interfacial charge extraction of new SAML-HSM/perovskite than classic spiro-OMeTAD layers.

To investigate the hole extraction in more detail, we performed energy-dispersive X-ray (EDX) mapping on the perovskite passivated by the new SAML-HSM (Figure 3c, left and Figure S4). The results clearly show good mixing between the diCNq-Aza species and the perovskite structure, indicating that SAML-HSM effectively passivates the hole traps and defects in the perovskite layer by diffusing into it.

To validate these findings, scanning electron microscopy (SEM) images of bare perovskite films and those containing diCNq-Aza are shown in Figure 3c (middle and right). The SEM images reveal a transition in surface morphology from spherical to needle-like structures, corresponding to an increase in the degree of crystallization.

In this area, time-resolved photoluminescence (TRPL) was used to shed light on the carrier extraction process through quantitative approaches [44,45]. As shown in Figure 3d new SAML-diCNq-Aza quenches the PL of the perovskite more effectively than spiro-OMeTAD. The calculated PL quenching factor (η_{quench}) for diCNq-Aza is 95% higher than that of spiro-OMeTAD of 93% (Table 1). Overall, PL measurements show that diCNq-Aza has more efficient hole extraction compared to spiro-OMeTAD.

To gain deeper insight into the electronic and geometric structure of diCNq-Aza, we applied the density functional theory (DFT) method with the Gaussian 09 program at B3LYP/6–31G level to optimize the ground-state geometry [46]. The optimized structures and energy levels of the frontier molecular orbitals for diCNq-Aza and spiro-OMeTAD are shown in Figures 3e and S4. Also, LUMO+1, LUMO, HOMO, HOMO-1, and HOMO-2 energy levels of diCNq-Aza and spiro-OMeTAD obtained from DFT calculations are shown in Figure S6 [47, 48].

As seen, the HOMO of diCNq-Aza is almost distributed over the electron donor moieties, while the LUMO is only localized on the anchoring groups, confirming the highest charge separation, which indicated that diCNq-Aza could be considered as an efficient D-A SAML-HSM in PSC. Furthermore, to get a deep understanding of the charge distribution of diCNq-Aza and determine the appropriate groups that bind to the perovskite surface, we performed an electrostatic surface potential (ESP) evaluation of the new SAML-HSM (Fig. 3f), which showed that the positive electrostatic potential is localized on the conjugated backbone. In contrast, the negative electrostatic potential corresponded to the strong electronegative ability of nitrogen atoms, which can serve as the Lewis base properties of the CN-anchoring group to passivate perovskite defects through the Pb atoms as a Lewis acid. In fact, remarkably, ESP clearly indicated that CN groups are able to act as Lewis bases to coordinate with Pb atoms as Lewis acid, confirming diCNq-Aza could be considered as a SAML-HSM.

View Article Online
DOI: 10.1039/D5TA02440D

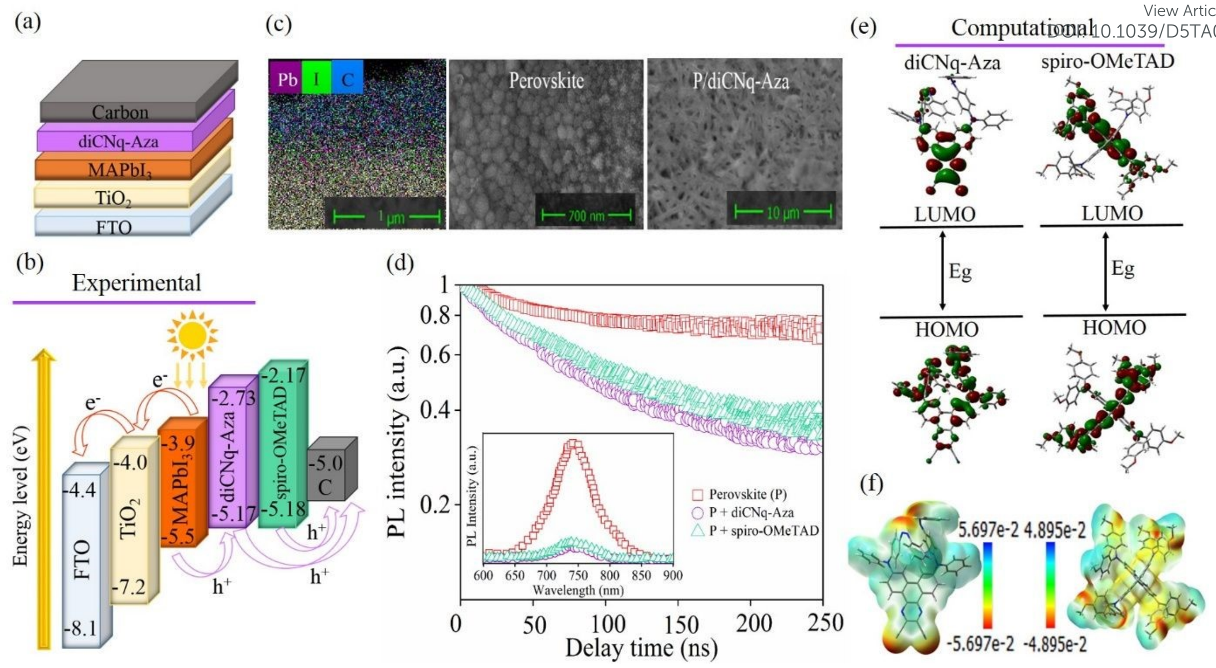

Figure 3. **(a)** Schematic structure of a perovskite solar cell device using diCNq-Aza as the HSM; **(b)** The relative energy levels in the PSCs based on diCNq-Aza and spiro-OMeTAD; **(c)** EDX map cross sectioanal (left) and Top view SEM images of the perovskite and p/diCNq-Aza layers of the device (right); **(d)** The corresponding PL decay curves measured at a wavelength near the band gap that yields the maximum PL signal upon exciting the perovskite, perovskite/diCNq-Aza and perovskite/spiro-OMeTAD and inset plot is the steady-state PL spectra of the perovskite and p/HSM films; **(e)** DFT calculated frontier molecular orbital distributions and energies of the HOMO and LUMO levels for diCNq-Aza and spiro-OMeTAD. Red and green represent electrons and holes, respectively; **(f)** Electrostatic surface potential (ESP) for HSM, regions of high and low potentials are indicated in red and blue, respectively.

In the following, to investigate the charge transfer of diCNq-Aza, the thermally activated hopping model under room temperature conditions is used. According to the Einstein-Smolochovsky equation [49], the hole mobility (μ) is given by:

$$\mu = \frac{e}{K_B T} D$$

where e is the elementary charge, and D is the diffusion coefficient, which can be evaluated from:

View Article Online
DOI: 10.1039/D5TA02440D

$$D = \lim_{t\to\infty} \frac{1}{2d}\frac{\langle x(t)^2\rangle}{t} \approx \frac{1}{2d}\sum_m r_m^2 K_m p_m$$

where d is the spatial dimensionality of the organic crystal (d = 3). $p_m = K_m/\sum_m K_m$ is the relative probability for a charge carrier to a particular mth neighbor. K_m is the hopping rate to the mth neighbor, which is obtained using the Marcus equation (refer to SI), and r_m is the centroid-to-centroid distance to the neighbor m. The values of hole mobility (μ_h), centroid-to-centroid distances (r_m), hole transfer integral (V_h), and the hole transfer rate are calculated for the stable dimer of the diCNq-Aza. According to the data in Table 2, the diCNq-Aza shows μ_h comparable to spiro-OMeTAD, and as a result, it works as an efficient HSM without extra doping [50, 51]. Table S1 in Supplementary Information presents the calculated values of solubility in chlorobenzene, chemical hardness, and dipole moments of diCNq-Aza and spiro-OMeTAD.

Table 2. Calculated Centroid-to-Centroid Distance (r_m), Hole Reorganization Energy (λ_h), Hole Transfer Integral (V_h), Hole Transfer Rate (k_h), and Hole Mobility (μ_h) of diCNq-Aza and spiro-OMeTAD.

HSM/HTM	r_m (Å)	λ_h (eV)	V_h (eV)	k_h (s^{-1})	μ_h (cm^2/Vs)
diCNq-Aza	13.08	1.0204	0.0731	4.588×10^9	0.45×10^{-3}
spiro-OMeTAD [52]	10.05	0.11	2.47×10^{-3}	3.77×10^{10}	2.47×10^{-3}

2.3 Surface morphology

The surface morphology and roughness of the perovskite films with and without HSM were studied by atomic force microscopy (AFM) [53]. As shown in the AFM topography, amplitude, and phase images in Figure 4, diCNq-Aza formed smooth, homogeneous and pin-hole-free thin films.

View Article Online
DOI: 10.1039/D5TA02440D

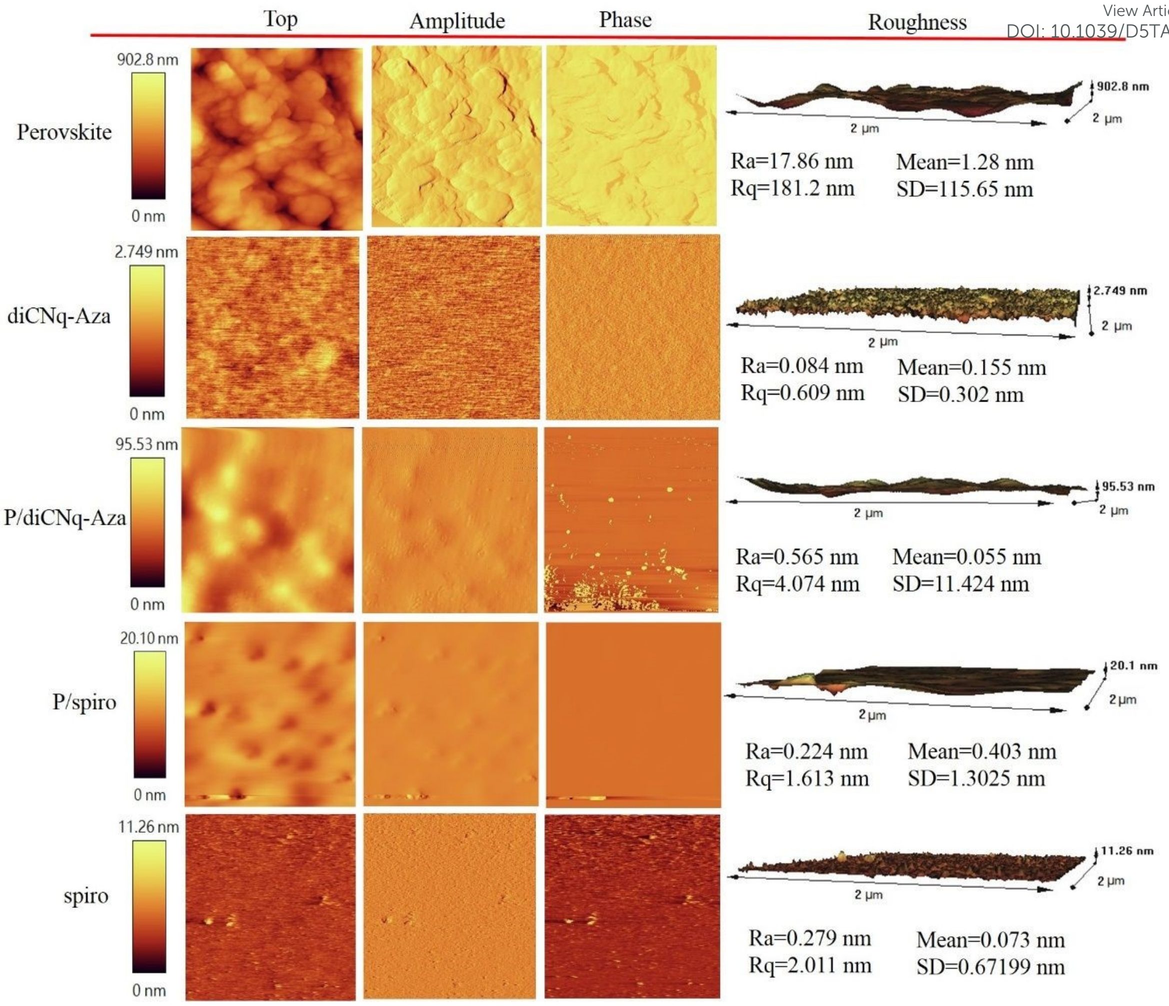

Figure 4. AFM topography. AFM photos of bare perovskite, diCNq-Aza, perovskite/diCNq-Aza, perovskite/spiro-OMeTAD and spiro-OMeTAD. Ra is average roughness, Rq is the root mean square roughness, and SD is the standard deviation of the profile heights.

The root means square roughness (Rq) values of the perovskite surface reduce from 181 nm in perovskite bare to 4 nm in perovskite/diCNq-Aza and likely the average roughness (Ra) reduces from 17 nm to 0.5 nm, suggesting the good film formation property of diCNq-Aza (which is important to prevent current leakage and facilitate better charge-collection efficiency in the PSCs). In fact, good morphological properties with a low surface roughness of new SAML-HSM in the solid thin-film form on a perovskite layer are desirable for hole extraction and transfer at the perovskite/SAML-HSM interface. Moreover, in Figure 4, the bottom part,

View Article Online
DOI: 10.1039/D5TA02440D

the relevant parameters for spiro-OMeTAD are shown for comparison with diCNq-Aza, and it can be seen that their values are close to each other [54].

2.4 The absorption energy of the diCNq-Aza/$CH_3NH_3PbI_3$ system is based on VASP calculations

To explore the possible pathways of the interaction of new SAML-HSM with the perovskite layer, the diCNq-Aza/$CH_3NH_3PbI_3$ system was geometrically optimized in Vienna ab initio simulation package (VASP) using projector-augmented wave methods with PBE generalized gradient approximation (GGA) exchange correlation [55, 56]. An energy cutoff of 400 eV was used, and the force convergence criterion for geometry optimization was set to 0.02 eVÅ^{-1}. Herein, a perovskite supercell was prepared as the adsorption surface.

In order to determine the most stable coordination mode of CN groups of diCNq-Aza on the perovskite surface, three different types of possible connections (modes 1-3, Figures 5 and S7) were suggested, which the corresponding adsorption energy (E_{ads}) and the distance between N atom in the diCNq-Aza, and Pb atom on the perovskite surface (*d*Pb-N) were computationally optimized.

By considering the various coordination modes of CN groups with Pb atoms of perovskite slab, surprisingly, our results indicated that bidentate bridging mode (1) and mono dentate mode (3) could efficiently bond to Pb atoms through the optimized bonding length of 2.67Å and 2.70 Å respectively, which are less than the sum of van der Waals radius of Pb and CN atoms. These interesting results clearly indicated an important hypothesis that the CN group via the N atom forms a new bond with the Pb atom of the perovskite surface and fills the iodine vacancy after adsorption on the crystal structure surface to reduce trap states on the perovskite surface [57].

The lone electron pairs on the N atom of diCNq-Aza can delocalize onto the 6p empty orbitals of Pb^{2+} to form coordination bonds with strong bonding strengths, while after optimizing mode

(2), named bidentate chelating, the bonding length increased to 2.84Å and 2.92Å, which rarely seen in the crystallographic literature [58].

In following, to find the most promising coordination mode based on the energy chemical absorption approach, the calculated E_{ads} (from the following equation) for mode1 and 3 were estimated at -1.04 eV and -1.12 eV, respectively, indicating the strong chemical adsorption of new SAML-HSM onto the perovskite surface.

$$E_{ads} = E_{total} - E_{\text{CH3NH3PbI3}} - E_{\text{diCNq-Aza}}$$

where E_{total}, $E_{\text{CH3NH3PbI3}}$, $E_{\text{diCNq-Aza}}$ denote the energy of diCNq-Aza/MAPbI$_3$ complex, MAPbI$_3$ and diCNq-Aza, respectively. In light of the above results, the amount of adsorption energy of mode (2) was calculated at about -0.122 eV, which is remarkably lower than modes 1 and 3. Thereby, the placement of diCNq-Aza on the perovskite in this mode is probably ruled out. It is also noteworthy that the number of optimization cycles of mode (1) is about half of mode (2) (47 and 87 cycles, respectively), which proves the earlier evidence. Obviously, herein, results clearly indicated that the newly molecular synthesized HSM could efficiently act as a SAML through the coordination of its two CN groups onto the surface of perovskite via one nitrogen atom of CN group to one Pb atom of perovskite, namely bidentate bridging (mode1).

The simulated charge transfer from the HSM to the perovskite, assessed in three different coordination modes, clearly demonstrates that varying these modes alters the amount of charge transfer. This observation confirms the strength of the interface interaction between the new HSM and the perovskite surface, as illustrated in Figure 5, where the size of the circles highlights this relationship. As detailed in the figure, the highest charge transfer occurs in the

View Article Online
DOI: 10.1039/D5TA02440D

bidentate bridging mode (mode 1), followed by the bidentate chelating mode (mode 2), and ultimately the mono dentate mode (mode 3) [59].

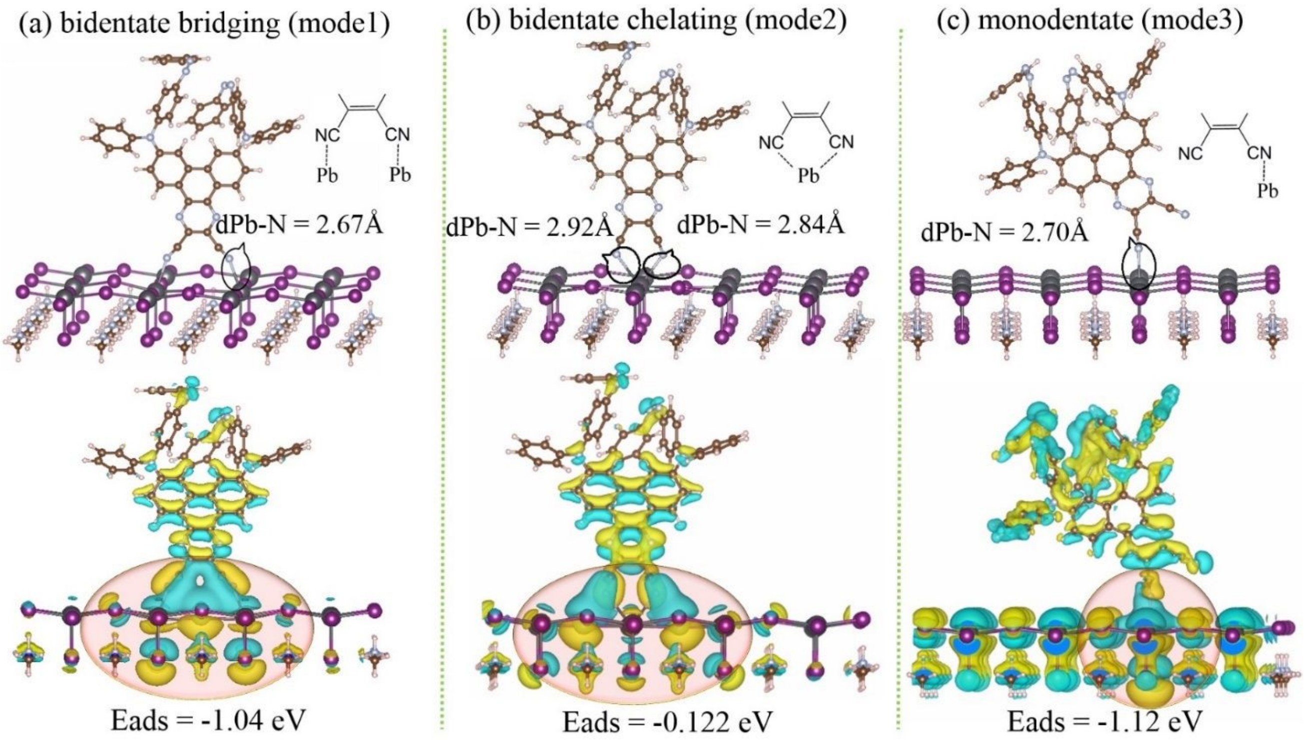

Figure 5. The optimized structures. The optimized structures of possible binding modes of diCNq-Aza on perovskite surface (up) and Charge density differences (CDD) for them (down), calculated adsorption energies (E_{ads}) are also shown. The yellow and blue regions represent charge accumulation and charge depletion in 3D space, respectively. The C, H, N, Pb, and I atoms are represented by brown, pink, blue, dark gray, and purple spheres, respectively.

2.5 Photovoltaic performance

For evaluation of the device performance of HSMs, the photocurrent density–voltage (J–V) characteristics of control and target devices (FTO/TiO_2/$MAPbI_3$/HSM/C) were investigated under AM 1.5 G irradiation at 100 mWcm^{-2}, and the current density-voltage (J-V) curves are shown in Figure 6a. The obtained parameters are summarized in Table 3 [60].

The photovoltaic performance of the new SAML-HSM showed better PCE value than benchmark spiro-OMeTAD through an open-circuit voltage (V_{OC}) of 1.16 V [61], a short circuit

View Article Online
DOI: 10.1039/D5TA02440D

current density (J_{SC}) of 22.27 mAcm^{-2} and a fill factor (FF) of 0.79, resulting a PCE of 20.37%, while, under the same condition, the PSC based on spiro-OMETAD PCE decreases to 19.33%. To our best knowledge, the obtained PCE of 20.37% is amongst the best values of PSC based on carbon cathode, which has been reported so far. radiative recombination due to the favor passivation of perovskite surface by CN groups, resulting the more efficient hole extraction by new SAML-HSM than classic spiro-OMeTAD. Moreover, as earlier shown based on XPS, FTIR and computational studies, the anchoring groups of diCNq-Aza coordinated into the surface of perovskite via the Pb atom, which stabilized the composite of diCNq-Aza/perovskite.

Given that the carbon electrode functions as an HSM, the new SAML-HSM was evaluated in a PSC incorporating a metal electrode. This assessment confirmed efficient hole mobility from the perovskite layer to the metal electrode. Notably, the carbon-PSC utilizing the new SAML-HSM exhibited only about 2% lower efficiency than the gold-PSC based on spiro-OMeTAD, indicating strong compatibility of the new diCN-HSM with the carbon electrode (data provided in Figure S8 in the Supporting Information).

Figure 6b illustrates the external quantum efficiency (EQE) curves for the devices based on new SAML-HSM and classic spiro-OMeTAD, which the integrated current density values (J_{SC}), calculated from the integration of the incident photon-to-electron conversion efficiency (IPCE) spectra were calculated 21.58 mA cm^{-2} and 22.48 mA cm^{-2}, respectively, which are almost in agreement with the values obtained from the J–V curves. Higher IPCE values of the device containing diCNq-Aza (93.24%) than the device with spiro-OMeTAD (86.41%) in the broad range of 400–750 nm, suggesting better charge carrier separation and hole extraction ability in new SAML-HSM. The PCE distribution and static data for 24 cells of diCNq-Aza and spiro-OMeTAD devices exhibited a narrow range which is comparable with silicon solar cells [61], which is shown in Figure S9.

View Article Online
DOI: 10.1039/D5TA02440D

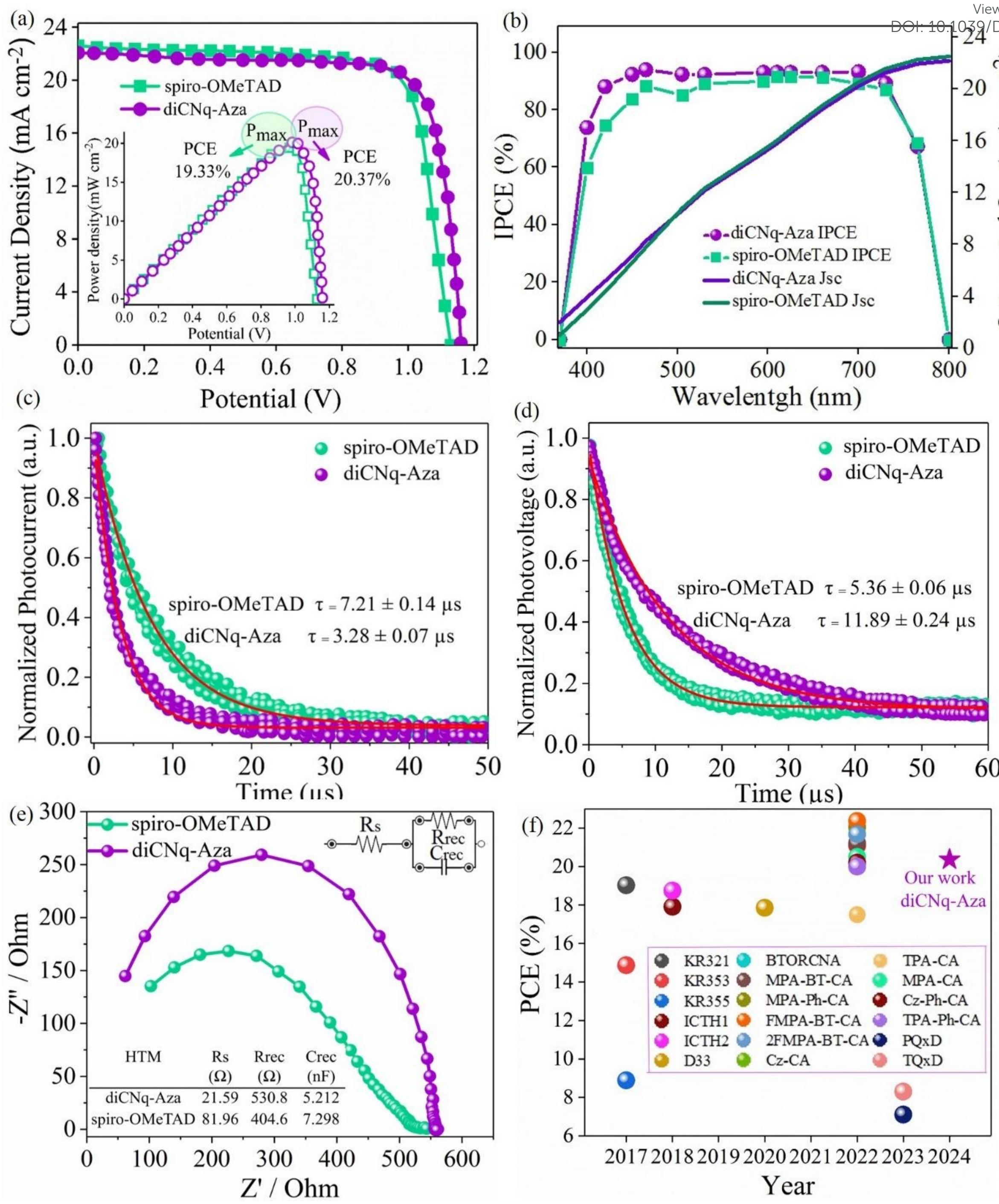

HTM	Rs (Ω)	Rrec (Ω)	Crec (nF)
diCNq-Aza	21.59	530.8	5.212
spiro-OMeTAD	81.96	404.6	7.298

Figure 6. **Photovoltaic performances of FTO/TiO$_2$/MAPbI$_3$/HSM/C system. (a)** J–V curves of the best-performing devices based on diCNq-Aza and spiro-OMeTAD (inset plot is the power density-voltage curve for these HSM-based systems); **(b)** IPCE spectra and integrated current curves of the corresponding devices; **(c)** The TPC and **(d)** The TPV curves of diCNq-Aza and spiro-OMeTAD based devices, respectively; **(e)** Nyquist plot (impedance spectra) and equivalent circuit for the film of perovskite with HSMs; **(f)** Comparison between PCEs for PSCs with SAML-HSMs reported in relevant

View Article Online
DOI: 10.1039/D5TA02440D

literature from 2017 to 2024 (The molecular structure of SAML-HSMs and the photovoltaic data are given in the Supplementary Information, Table S4, Fig S10).

Table 3. Photovoltaic parameters of PSCs ($FTO/TiO_2/MAPbI_3/HSM/C$) based on diCNq-Aza and spiro-OMeTAD

HSM/HTM	J_{SC} (mA cm^{-2})	V_{OC} (V)	FF (%)	PCE (%)
diCNq-Aza	22.27	1.16	78.85	20.37
spiro-OMeTAD	22.60	1.13	75.69	19.33

We have used the transient photocurrent (TPC) and the transient photovoltage (TPV) techniques to investigate the mechanisms of charge extraction and non-radiative recombination in the novel SAM-based perovskite solar cells. TPC technique, which measures the change in photocurrent passing through the device, is related to the measurement of charge carrier transport, and TPV technique is related to the charge carrier recombination [62]. The charge carrier extraction was determined using a single exponential fit to the TPC curves, and the device lifetime was determined using a double exponential fit to the TPV curves. The fitting results are listed in Table S2 [63, 64] . As can be seen from Figures 6c and 6d, the cell with diCNq-Aza exhibits faster decay and shorter charge extraction time ($\tau = 3.28$ μs) compared to the spiro-OMeTAD ($\tau = 7.21$ μs) containing cell, confirming the more efficient extraction of charge carriers in this cell. Surprisingly, the new SAM-based device has a longer carrier lifetime at 11.89 μs compared to 5.36 μs for the control device, indicating better suppression of non-radiative recombination.

To gain deeper insight into the interfacial charge transfer and recombination processes at the perovskite/HSM interface, we conducted electrochemical impedance spectroscopy (EIS) measurements on PSCs. The Nyquist plot and the corresponding equivalent circuit are presented in Figure 6e, with detailed data provided in Table S3. Each circuit features a series

View Article Online
DOI: 10.1039/D5TA02440D

resistance (Rs) attributed to the contact resistance of the electrical wire and fluorine-doped tin oxide (FTO) electrode, which can be determined from the high-frequency intercept on the real axis. Notably, the new self-assembled monolayer HSM diCNq-Aza exhibits a low Rs of 21.59 Ω, indicating effective passivation of perovskite surface defects and optimal interfacial contact, contributing to an increased FF as observed in the photovoltaic performance. Additionally, the arc diameter in the Nyquist plot, which can be accurately fitted using the equivalent circuit, is indicative of the recombination process and consists of two components: recombination chemical capacitance (C_{rec}) and recombination resistance (R_{rec}). The higher $\mathrm{R_{rec}}$ value of 530.8 Ω for diCNq-Aza versus spiro-OMeTAD (404.6 Ω) signifies reduced recombination and enhanced charge transport, attributed to improved film quality and fewer defects, resulting in higher $\mathrm{V_{OC}}$ and FF [65, 66]. To provide a clear overview of the photovoltaic performance of the new SAML-HSM, Figure 6f and Table S4 present a historical comparison of PCEs for PSCs with various SAML-HSMs containing CN and CNCOOH groups, as reported in the literature from 2017 to 2024 [58, 67-73] (molecular structures are shown in Figure S10). The highest PCE values reported for these PSCs, using metal cathode electrodes, range from 22% to 23%. Surprisingly, the PCE of the diCNq-Aza SAML-HSM reached 20.37% when using carbon electrodes, which is competitive with metal cathode-based devices. Notably, literature on PSCs with HSMs and carbon electrodes is limited, as C-PSCs typically function without HSMs. This underscores the potential of C-PSCs based on SAML-HSMs as promising alternatives to metal-based PSCs, particularly those with gold cathodes. This work reports the first efficient PSC based on SAML-HSMs containing CN groups as anchoring sites, achieving a PCE greater than 20%.

View Article Online
DOI: 10.1039/D5TA02440D

2.6 Device Stability

Lastly, the stability of our C-PSCs based on new SAML is preliminarily evaluated through thermal aging and shelf-life aging, showing satisfactory performance even without encapsulation. To shed light on the photostability behavior of new diCNq-Aza as SAML-HSM, the long-term stability at room temperature was tested. Photocurrent–voltage (*J–V*) characteristics of the devices were measured under standard conditions at simulated AM 1.5G sunlight. As can be seen in Figure 7a, the efficiency of the new SAML-HSM keeps the maximum value of 20.61 in the first 50 hours, and in the next 200 hours, we see a slow decline, which increases again in the following hours, and finally, after 600 h of aging, the PCE still retained 93.32% (19.01) of its initial PCE value. Surprisingly, the PCE values of PSCs based on classic spiro-OMeTAD dramatically decreased within the first 50h, which continued by about 400 hours, and finally, a drop of the PCE to 65.91% (12.74) of the initial value was observed at the end of 600 hours. In fact, as clearly shown in Figure 7a, based on the highlighted sub-area schematic, which defines the loss of PCE over time, newly designed SAML-HSM indicated a much lower PCE loss than spiro-OMeTAD, indicating an excellent photostability of diCNq-Aza over time. The inset plot of Figure 7a confirms that about 400 hours (60%) of total left time under illumination, the PCE of the new HSM was maintained in the range of 19-19.5%, while the spiro-OMeTAD indicates efficiency in the range of 14.5-15% for about 50% of the duration time. Statistical stability data of J_{sc}, V_{oc}, FF, and PCE for the PSCs based on diCNq-Aza and spiro-MeOTAD are collected in Table S5.

Further investigations were conducted to assess the thermal stability of the device over a range of temperatures from 25 °C to 100 °C, aiming to understand the effects of temperature combined with illumination on system stability (Fig. 7b). With the exception of 60 °C, both devices exhibited similar performance trends at other temperatures. Notably, when the PSC based on diCNq-Aza was maintained at 60 °C, the PCE increased to 22.42%, representing approximately a 10% improvement compared to the same PSC at 25 °C. This suggests that elevated temperatures can effectively enhance PCE over time. Higher temperatures positively impact PCE by improving the crystallinity of the perovskite, thereby enhancing charge mobility and facilitating more efficient hole extraction [74-77].

Figure 7c displays the thermal stability of the new self-assembled monolayer HSM at 80 °C, with diCNq-Aza showing a PCE of 19.62%, while spiro-OMeTAD exhibited a decline to 15.75%. Notably, after 100 hours at this temperature, the maximum PCE values for both HSMs reached approximately 20.82% for diCNq-Aza and 20.35% for spiro-OMeTAD. Interestingly, the PCE values increased by about 6% and 29% from their initial readings for diCNq-Aza and spiro-OMeTAD, respectively. During the subsequent 100 hours, diCNq-Aza maintained PCE close to its original value, demonstrating stable performance, ultimately showing 97.45% of its initial efficiency at 600 hours. In contrast, the spiro-OMeTAD system exhibited marked fluctuations in efficiency between 100 and 600 hours, experiencing a rapid decline after reaching its maximum PCE and ending at 73.52% of its initial efficiency. To our knowledge, this thermal stability behavior is among the best documented for organic HSM-based PSCs to date. For additional photovoltaic data related to temperature stability at 80 °C, please refer to Table S6.

The photo and thermal stability of PSCs based on diCNq-Aza significantly exceed those of spiro-OMeTAD. This enhanced stability can be attributed to the strong Pb-N interactions between the SAML-HSM and the perovskite, which effectively passivate defects within the perovskite layer. These results underscore the essential role of diCNq-Aza in protecting the perovskite device from degradation. Figure 7d illustrates that the new SAML featuring a C-N anchoring group exhibits the highest thermal stability over time at 80 °C compared to other SAML families, with additional details of the molecular structures summarized in Table S7.

View Article Online
DOI: 10.1039/D5TA02440D

One-year photographic stability. The stability of an HSM is a critical factor for industrialization and commercialization. In this study, the photostability of the thin film of the new SAML-HSM applied to the perovskite layer was monitored for one year under ambient conditions without encapsulation (see Fig. S11).

Figure 7e displays images of PSC films, illustrating color changes over time. This straightforward and effective stability test involves monitoring the transition between two contrasting colors: dark brown, representing the perovskite, and yellow, denoting decomposed perovskite. The color analysis was conducted using "Extract Colors from Image" software, where the extracted colors correlate to the year-long study, with the numbers on the color bars indicating the percentage of each color present in the films. As shown in Figure 7e, the unprotected perovskite film began to change from dark brown to yellow within two months of light exposure, indicating degradation into PbI_2. In contrast, the color change in the diCNq-Aza-containing perovskite film was minimal; after two months, this film exhibited nearly 100% retention of its original color. The compositional images of the aging perovskite combined with the new SAML indicate that approximately 90% of the original color was retained after nine months, confirming the remarkable stability of the diCNq-Aza SAML-HSM perovskite interface over an extended period.

View Article Online
DOI: 10.1039/D5TA02440D

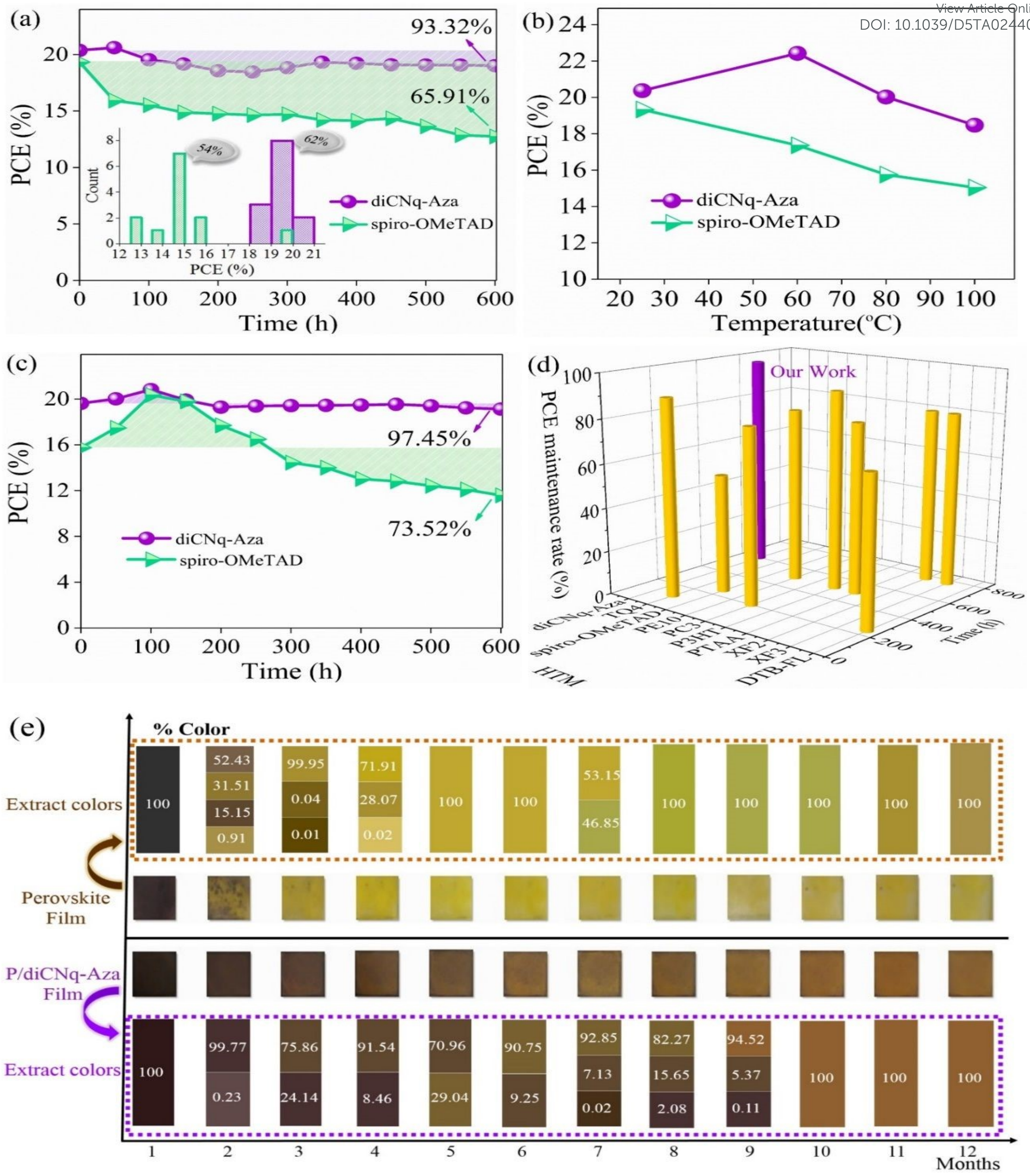

Figure 7. Stability measurements, aging test results of PSCs (FTO/TiO$_2$/MAPbI$_3$/HSM/C) containing HSMs. (a) Long term photo stability of diCNq-Aza and spiro-OMeTAD based PSCs at 25 °C (The inset plot is a column chart of multiple times with the same PCE%); **(b)** The PCE changes at 4 incremental temperatures; **(c)** Long-term thermal stability at 80 °C; **(d)** PCE maintenance rate (%) in PSCs based on different HSMs based literature; **(e)** Stability test photos of fresh and aged films at regular intervals under ambient conditions with a temperature of 25^{o}C for one year. Up: Films and color

View Article Online
DOI: 10.1039/D5TA02440D

bars of perovskite, Down: Films and color bars of perovskite with diCNq-Aza. The colors are extracted from the images, and the numbers written in the color bars show the percentage of different colors in the films.

2.6 Estimating the cost of producing new HSM and comparing it with other HSM/HTMs

An important advantage of the new SAML-HSM compared with spiro-OMeTAD is the much lower synthesis cost. The synthesis cost of 1 gram of diCNq-Aza was estimated according to the cost models of Petrus et al., and Osedach et al.,[78] and compared with the price of 1 gram spiro-OMeTAD . The prices of the materials used were obtained from Sigma-Aldrich. In summary, the estimated cost of diCNq-Aza is 27.5 $\$g^{-1}$ (Table S8) which is a 10-fold reduction compared to the cost of spiro-OMeTAD (273.$ g^{-1}) [79, 80]. In addition, to compare the price of the new SAML-HSM with spiro-OMeTAD at different PCEs of corresponding PSCs, the cost per peak watt was calculated using the following equation [81], where η is the solar cell efficiency (PCE%) in the range of 2–30%, C_g is the cost per gram, ρ is the density, which is assumed to be 1.1 g/cm^3, t is the thickness of the donor material, which is assumed to be 100 nm and I is the solar irradiance at peak conditions, which is assumed to be 1000 W/m^2. $C_W = \frac{C_g * \rho * t}{\eta * I}$

According to the Figure 8a, C_W as a function of PCE, shows that the cost of preparing diCNq-Aza is much more economical than spiro-OMeTAd. The values mentioned inside the graph are the costs per watt peak in the PCEs obtained for HSM/HTMs in this study (photovoltaic section), where the cost value at PCE = 20.37% is equal to 0.15 $\$/W_p$, which is more than ten times lower compared to 1.56 $\$/W_p$ for spiro-OMeTAD at PCE = 19.33%.

In particular, given that the type of cathode electrode used also has a significant impact on the cost of a solar cell, a comparison was made between the price of a conventional gold electrode and the carbon electrode used in this study. Specifically, carbon paste costs between €10 and €100 per kg, and 20 g/m² is required to deposit a 20 μm carbon film. This results in a

View Article Online
DOI: 10.1039/D5TA02440D

final cost of approximately €0.20 to €2.00 per m² for the carbon electrode. In contrast, the cost of a gold electrode, assuming a thickness of 100 nm and current gold prices of €55 to €60 per gram, ranges from €1062 to €1159 per m². Figure 8b shows the graph of the cost changes in grams for producing one gram of the new SAML-HSM and one gram of spiro-OMeTAD in a PSCs with two different types of carbon and gold electrodes. Since other cell components are constant in all the desired PSCs, their costs are not included and the reported costs are the sum of the price of one gram of electrode and one gram of HSM/HTM. Four different compounds of two types of electrodes (carbon and gold) and two different HSM/HTMs were systematically compared, C/diCNq-Aza, Au/diCNq-Aza, C/spiro-OMeTAD and Au/spiro-OMeTAD. The expected cost values for these four combinations are 27.51, 90.75, 273.61 and 336.85 $ per gram, respectively, and are shown in the Figure 8b. As can be seen, changing the electrode from carbon to gold and keeping the HSM constant results in a cost increase of more than 63 $, as well when the carbon electrode is fixed and the HSM changed from diCNq-Aza to spiro-OMeTAD, there is an increase of about 246 $ was observed. The significant difference in cost is when the carbon electrode is replaced with gold electrode and the new SAML-HSM with spiro-OMeTAD, which results in a cost increase of about 310 $. This large difference in price definitely justifies and proves the economic viability of the proposed cell based on carbon cathode and new molecule.

In addition to spiro-OMeTAD, other small organic HTM/HSMs can be compared to diCNq-Aza in terms of synthesis cost and PCE of the corresponding cells (Figure 8c). In a short comparison between the new proposed HSM and ten other HTMs mentioned in previous studies, the new HSM had the lowest production cost in dollars per gram, with a PCE almost equivalent to the highest PCEs which reported so far.

View Article Online
DOI: 10.1039/D5TA02440D

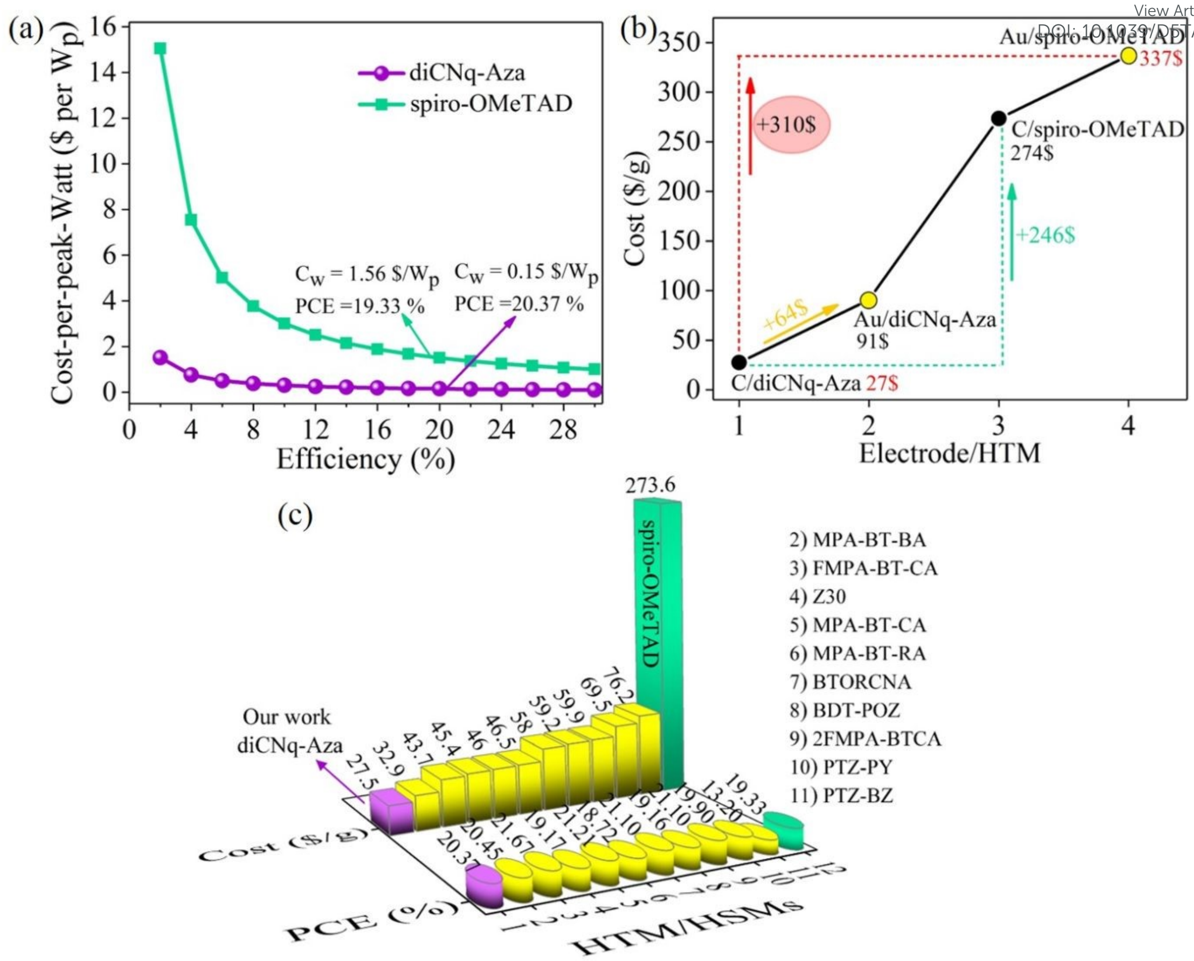

Figure 8. Cost estimates. (a) Cost per peak watt ($/Wp) for diCNq-Aza and spiro-OMeTAD; **(b)** Graph of changes and comparison of costs in gram for PSCs with carbon or gold as electrodes and diCNq-Aza or spiro-OMeTAD as HSM/HTM; **(c)** Comparison between costs and PCEs of PSCs with different HTSM/HTMs, as reported in our work and other relevant studies. The HSM/HTMs are named with numbers from 1 to 12. Their full names are listed in a column next to the chart.

3. Conclusion

The newly designed diCNq-Aza, as a SAML-HSM, demonstrates significant potential for efficient carbon electrode PSCs. The functional CN group, conjugated with π-extended Aza units, acts as an effective anchoring group that binds to the perovskite surface. Our results show that the SAML-HSM layer facilitated the formation of a uniform perovskite nanocrystal layer with excellent crystallinity, morphology, and minimal roughness. The interaction between the CN group and Pb^{2+} ions reduces surface defect densities and minimizes energetic mismatches

View Article Online
DOI: 10.1039/D5TA02440D

between the perovskite and HSM. Based on calculated absorption energies for different connection modes, we identified the bidentate bridging configuration (mode 1) as the most stable and favorable. Notably, the PSC utilizing the carbon electrode achieved a PCE of 20.37%, surpassing that of spiro-OMeTAD-based devices and ranking among the highest reported values for carbon-based PSCs. Moreover, the photo-thermal stability of the PSC with the new SAML-HSM retained over 95% of its initial performance at 80 °C, demonstrating exceptional thermal resilience for carbon-based PSCs. Remarkably, after nearly one year, the PSC exhibited no visible degradation, whereas the unmodified perovskite collapsed within one month. Our findings pave the way for market-competitive carbon-based PSCs by integrating the new C-N functionalized SAML-HSM with carbon electrodes.

Moreover, the cost-effective PSC utilizing diCNq-Aza SAML-HSM with a carbon cathode reduces the overall production costs while facilitating easier layer deposition, thereby achieving three key benefits: (1) high efficiency (over 20% PCE), (2) high stability (more than 90% retention), and (3) low cost. Substantial cost difference highlights the significant economic advantage of using carbon-based electrodes in PSCs, particularly for large-scale production where cost efficiency is essential.

Experimental

Synthetic procedures of the target HSM: diCNq-Aza was successfully synthesized via two simple steps and was purified by recrystallization and column chromatography. The molecular structures and synthetic routes are shown in Figure 1. diCNq-Aza was thoroughly characterized by FT-IR, ^{1}H-NMR, and ^{13}C-NMR spectroscopy, and the obtained results were found to be consistent with the proposed molecular structure.

Synthesis of 7,10-dibromo benzo [f.h] quinoxaline-2,3-dicarbonitrile (3 in Fig. 1): At first, 0.22g (0.6 mmol) of (3,6-dibromophenanthrene-9,10-dione) (1 in Fig. 1) and 0.064g (0.6 mmol)

View Article Online
DOI: 10.1039/D5TA02440D

of (2,3-diaminomaleonitrile) (2 in Fig. 1) were weighed and poured into a 25 ml flask and then 10 ml of acetic acid was added to them. The resulting mixture was refluxed for 8 hours under a nitrogen atmosphere at a temperature of 127°C. After cooling down to ambient temperature, the reaction product was added to cold distilled water, and the precipitate was filtered and washed with distilled water several times (~91% yield). ^{1}H-NMR (250 MHz, $CDCl_3$); δ=9.04(d,2H); 8.7(d,2H); 7.96(dd,2H). CHN: Anal. calcd. For $C_{18}H_6Br_2N_4$, (%): C, 49.352; H, 1.383; Br, 36.475, N, 12.79, ESI-MS: m/z, 434.721, [M-H] +.

Synthesis of 7,10-bis(phenyl(4-((E) phenyldiazenyl) phenyl) amino) dibenzo[f,h] quinoxaline -2,3-dicarbonitrile (diCNq-Aza): A mixture of CuI (0.050 g), 1,10-phenanthroline (0.10 g), Cs_2CO_3 (2.00 g), 3 in Figure 1 (0.44 g, 1 mmol), 4-phenylazo diphenylamine (4 in Fig. 1) (0.546 g, 2 mmol) and 5 ml of dimethylformamide (DMF) was heated under refux for 72 h under a nitrogen atmosphere at a temperature of 150°C. After cooling to ambient temperature, the product was extracted by using CH_2Cl_2 and H_2O. The combined organic phases were dried over anhydrous $MgSO_4$ and evaporated (85 % yield). ^{1}H-NMR (250 MHz, $CDCl_3$); δ=6.9-7.15(m,6H), 7.19 7.32(m,10H), 7.47-7.50(m,6H), 7.76-7.90(m,8H), 8.26(d,2H), 8.82(d,2H). CHN: Anal. calcd. For $C_{54}H_{34}N_{10}$ (%): C, 78.813; H, 4.166; N, 17.027. ESI-MS: m/z,821.29, [M-H] +.

Fabrication of PSCs. First, small glass slices coated with fluorine-doped tin oxide (FTO) were etched with zinc powder and HCl 2 M in deionized water to be used as a substrate for making solar cells. Then, the substrates were cleaned with detergents and deionized water and were washed in 4 stages of washing respectively in deionized water, 0.1 M HCl solution in ethanol, acetone, and ethanol, using ultrasonic waves. Next, on these substrates, mesoporous TiO_2 layers (150-200 nm) were deposited with a spin coating of TiO_2 paste diluted with absolute ethanol in a volume ratio of 1:8 at 2000 rpm for 10 seconds. To prepare $MAPbI_3$, 460 mg of lead(II) iodide (PbI_2) and 300 mg of methyl ammonium iodide (MAI) were separately in 1 mL of N, N-dimethylformamide (DMF) and isopropanol alcohol, respectively. Then, the PbI_2 solution was spin-coated at 3200 rpm for 20 s on the mesoporous TiO_2 layers. The Samples were annealed at 100°C for 10 min. After cooling, the MAI solution was spin-coated on the PbI_2 films at 3200 rpm for 20 s. Finally, the $MAPbI_3$ layers were heated at 100°C for 10 min. The substrates were then annealed at 100 °C for 1 h on the hot plate. The HSM solution was prepared by dissolving the HSMs in chlorobenzene. Then 18 ml LiTFSI (from a stock solution in acetonitrile with a concentration of 1.0 M) and 29 ml tert-butyl pyridine (from a stock solution in chlorobenzene with a concentration of 1.0 M) were added to the spiro-OMeTAD solution. The HSM was applied onto the perovskite film through spin coating using the HSM solutions at a speed of 4000 rpm for 20 s. Subsequently, the substrates were dried at 100° C for 5 min. Finally, the C cathode were deposited by the doctor, blading the corresponding pastes, which were dried at 100°C for 30 min [82].

Acknowledgments

S.R. and H.S. thank the University of Zanjan for financial support and thank Mohammadreza Hosseini for his helpful guidance in the computational section.

Abbreviations

SAML, Self-assembled molecular layer; HSM, Hole-selective material; PSC, Perovskite solar cell; PCE, Power conversion efficiency; VASP, Vienna ab initio simulation package; E_{ads}, Adsorption energy; Spiro-OMeTAD, 2,2',7,7'-tetrakis(N,N-di-p-methoxyphenylamine)-9.9'-spirobifluorene; ISOS-D-1, Thermal aging and shelf-life aging; HTM, Hole transport material; HSM, Hole-selective materials; FF, Fill factor; V_{OC}, Open-circuit voltage; PA, Phosphonic

View Article Online
DOI: 10.1039/D5TA02440D

acid; CA, Carboxylic acid; CAA, Cyanoacetic acid; SI, Supplementary Information; D-π-A, Donor-π-acceptor; diCNq-Aza, 7,10-bis(phenyl(4-((E)phenyldiazenyl) phenyl) amino) dibenzo[f,h] quinoxaline -2,3-dicarbonitrile; SAML-HSM, SAML-type HSM; LITFSI, Lithium bis(trifluoromethanesulfonyl)imide; Cs_2CO_3, Cesium carbonate; CuI, Copper iodide; UV-Vis, Ultraviolet-visible; PL, Photoluminescence; λ_{max}, Maximum wavelength; E_g, Optical band gap; , em, emission; E_{LUMO}, Lowest unoccupied molecular orbital energy; CV, Cyclic voltammetry; E_{HOMO}, Highest occupied molecular orbital energy; ΔG, Formation energy; T_g, Glass transition temperature; DSC, Differential Scanning Calorimetry; C-PSC, carbon-based perovskite solar cell; EDX, Energy-dispersive X-ray; SEM , Scanning electron microscopy; TRPL, time-resolved photoluminescence; η_{quench}, PL quenching factor; DFT, Density functional theory; VB, Valence band; CB, Conduction band; ESP, Electrostatic surface potential; μ_h, Hole mobility; AFM, Atomic force microscopy; Rq, Root mean square roughness; Ra, Average roughness; SD, Standard deviation of the profile height; GGA, Generalized gradient approximation; E_{ads}, Adsorption energy; $MAPbI_3$ ($CH_3NH_3PbI_3$), Methyl ammonium lead iodide; FTO, Fluorine doped tin oxide; TiO_2, Titanium dioxide; J-V, Current density-voltage, J_{SC}, Short circuit current density; EQE, External quantum efficiency; IPCE, Incident photon-to-electron conversion efficiency; EIS, Electrochemical impedance spectroscopy; Rs, Series resistance; C_{rec}, Recombination chemical capacitance; R_{rec}, Recombination resistance; P, Perovskite; PbI_2, Lead iodide; FT-IR, Fourier transform infrared; ^{1}H-NMR, Proton nuclear magnetic resonance; ^{13}C-NMR, Carbon 13 nuclear magnetic resonance; $CDCl_3$, Deuterated chloroform; MHz, Megahertz; Anal. Calcd, calculated values of the percentage composition of a compound based on its molecular formula; ESI-MS, Electrospray ionization mass spectroscopy; DMF, Dimethylformamide; CH_2Cl_2: Dichloromethane; $MgSO_4$: magnesium sulfate; MAI, Methylammonium iodide; XPS; X-ray photoelectron spectroscopy; TPC; transient photocurrent technique; TPV; transient photovoltage.

View Article Online
DOI: 10.1039/D5TA02440D

Synopsis

Introduction and design of a new SAM-HSL (diCNq-Aza) for a carbon based perovskite solar cell and comparison of the power conversion efficiency of this device with the PCE of C-PSC based on spiro-OMeTAD as a HTM.

References

1. S.-H. Turren-Cruz, M. Saliba, M. T. Mayer, H. Juárez-Santiesteban, X. Mathew, L. Nienhaus, W. Tress, M. P. Erodici, M.-J. Sher and M. G. Bawendi, *Energy Environmental Science*, 2018, **11**, 78-86.
2. Z. Zhu, D. Zhao, C.-C. Chueh, X. Shi, Z. Li and A. K.-Y. J. J. Jen, *Joule*, 2018, **2**, 168-183.
3. A. Farokhi, H. Shahroosvand, G. Delle Monache, M. Pilkington and M. K. J. C. S. R. Nazeeruddin, *Chemical Society Reviews*, 2022, **51**, 5974-6064.
4. F. Ali, C. Roldán-Carmona, M. Sohail and M. K. J. A. E. M. Nazeeruddin, *Advanced Energy Materials*, 2020, **10**, 2002989.
5. Q. Jiang, R. Tirawat, R. A. Kerner, E. A. Gaulding, Y. Xian, X. Wang, J. M. Newkirk, Y. Yan, J. J. Berry and K. J. N. Zhu, *Nature*, 2023, **623**, 313-318.
6. C. Li, Y. Chen, Z. Zhang, C. Liu, F. Guo, W. Ahmad and P. Gao, *Energy & Environmental Science*, 2024, **17**, 6157-6203.
7. C. Li and P. Gao, *Chinese Journal of Structural Chemistry*, 2024, 100324.
8. Q. Jiang and K. J. N. R. M. Zhu, *Nature Reviews Materials*, 2024, 1-21.
9. S. Y. Kim, S. J. Cho, S. E. Byeon, X. He and H. J. J. A. E. M. Yoon, *Advanced Energy Materials*, 2020, **10**, 2002606.
10. E. Yalcin, M. Can, C. Rodriguez-Seco, E. Aktas, R. Pudi, W. Cambarau, S. Demic and E. J. E. E. S. Palomares, *Energy Environmental Science*, 2019, **12**, 230-237.
11. A. Ullah, K. H. Park, Y. Lee, S. Park, A. B. Faheem, H. D. Nguyen, Y. Siddique, K. K. Lee, Y. Jo and C. H. J. A. F. M. Han, *Advanced Functional Materials*, 2022, **32**, 2208793.
12. S. Casalini, C. A. Bortolotti, F. Leonardi and F. J. C. S. R. Biscarini, *Chemical Society Reviews*, 2017, **46**, 40-71.

13. E. Li, C. Liu, H. Lin, X. Xu, S. Liu, S. Zhang, M. Yu, X. M. Cao, Y. Wu and W. H. J. A. F. M. Zhu, *Advanced Functional Materials*, 2021, **31**, 2103847.

14. Y. Yao, C. Cheng, C. Zhang, H. Hu, K. Wang and S. J. A. M. De Wolf, *J Advanced Materials*, 2022, **34**, 2203794.

15. Y. Lin, Y. Firdaus, F. H. Isikgor, M. I. Nugraha, E. Yengel, G. T. Harrison, R. Hallani, A. El-Labban, H. Faber and C. J. A. E. L. Ma, *J ACS Energy Letters*, 2020, **5**, 2935-2944.

16. Z. Zhang, L. Qiao, K. Meng, R. Long, G. Chen and P. J. C. S. R. Gao, *J Chemical Society Reviews*, 2023, **52**, 163-195.

17. S. N. Afraj, A. Velusamy, C.-Y. Chen, J.-S. Ni, Y. Ezhumalai, C.-H. Pan, K.-Y. Chen, S.-L. Yau, C.-L. Liu and C.-H. J. J. o. M. C. A. Chiang, *Journal of Materials Chemistry A*, 2022, **10**, 11254-11267.

18. K. Wang, J. Liu, J. Yin, E. Aydin, G. T. Harrison, W. Liu, S. Chen, O. F. Mohammed and S. J. A. F. M. De Wolf, *Advanced Functional Materials*, 2020, **30**, 2002861.

19. K. Sanusi, A. O. Olukoya, N. O. Sanyaolu, A. A. Ibikunle, S. T. Yussuf, S. A. Ogundare, N. O. Fatomi, O. C. Atewolara-Odule and P. B. J. J. o. F. Khoza, *Journal of Fluorescence*, 2024, 1-13.

20. N. Gu, Y. Feng, L. Song, P. Zhang, P. Du, L. Ning, Z. Sun, H. Jiang and J. J. J. o. M. C. C. Xiong, *Journal of Materials Chemistry C*, 2023, **11**, 8942-8951.

21. Q. Liao, Y. Wang, Z. Zhang, K. Yang, Y. Shi, K. Feng, B. Li, J. Huang, P. Gao and X. Guo, *Journal of Energy Chemistry*, 2022, **68**, 87-95.

22. T. Niu, W. Zhu, Y. Zhang, Q. Xue, X. Jiao, Z. Wang, Y.-M. Xie, P. Li, R. Chen and F. J. J. Huang, *Joule*, 2021, **5**, 249-269.

23. Y. Hua, B. Xu, P. Liu, H. Chen, H. Tian, M. Cheng, L. Kloo and L. J. C. S. Sun, *Chemical Science*, 2016, **7**, 2633-2638.

24. C. Igci, S. Paek, K. Rakstys, H. Kanda, N. Shibayama, V. Jankauskas, C. Roldán-Carmona, H. Kim, A. M. Asiri and M. K. J. S. R. Nazeeruddin, *Solar Rrl*, 2020, **4**, 2000173.

25. M. Jeong, I. W. Choi, E. M. Go, Y. Cho, M. Kim, B. Lee, S. Jeong, Y. Jo, H. W. Choi and J. J. S. Lee, *Science*, 2020, **369**, 1615-1620.

26. D. R. Kil, C. Lu, J.-M. Ji, C. H. Kim and H. K. J. N. Kim, *Nanomaterials*, 2020, **10**, 936.

27. L. Qian, S. Fu, S. Li, R. Miao, X. Feng, W. Zhang, Z. Xiao, W. Wang and W. J. J. o. M. S. M. i. E. Song, *Journal of Materials Science: Materials in Electronics*, 2022, **33**, 18028-18038.

28. R. Chen, B. Long, S. Wang, Y. Liu, J. Bai, S. Huang, H. Li, X. J. A. A. M. Chen and Interfaces, *ACS Applied Materials*, 2021, **13**, 24747-24755.

29. X. Liu, B. Ding, M. Han, Z. Yang, J. Chen, P. Shi, X. Xue, R. Ghadari, X. Zhang and R. J. A. C. Wang, *Angewandte Chemie*, 2023, **135**, e202304350.

30. R. Singh, K. Sharma, S. B. Elavarasi, M. J. O. Guin and Q. Electronics, *Optical Quantum Electronics*, 2024, **56**, 1002.

31. E. Rezaee, D. Khan, S. Cai, L. Dong, H. Xiao, S. R. P. Silva, X. Liu and Z.-X. J. M. C. F. Xu, *Materials Chemistry Frontiers*, 2023, **7**, 1704-1736.

32. W. Li, W. Zhao, K. Li and X. J. J. o. M. C. C. Han, *Journal of Materials Chemistry C*, 2023.

33. H. Luo, Z. Zhang, L. Yuan, J. Wang, B. Li, S. Wang, M. Abdi-Jalebi, L. Shi, W. Zhang and K. J. C. N. Guo, *Carbon Neutrality*, 2023, **2**, 21.

34. H. Zhu, Z. Shen, L. Pan, J. Han, F. T. Eickemeyer, Y. Ren, X. Li, S. Wang, H. Liu and X. J. A. E. L. Dong, *ACS Energy Letters*, 2020, **6**, 208-215.

35. B. Pashaei, S. Bellani, H. Shahroosvand and F. J. C. S. Bonaccorso, *Chemical Science*, 2020, **11**, 2429-2439.

36. M. Jeong, I. W. Choi, K. Yim, S. Jeong, M. Kim, S. J. Choi, Y. Cho, J.-H. An, H.-B. Kim and Y. J. N. P. Jo, *Nature Photonics*, 2022, **16**, 119-125.

37. P. J. S. Rana, R. K. Gunasekaran, S. H. Park, V. Tamilavan, S. Karuppanan, H.-J. Kim and K. J. T. J. o. P. C. C. Prabakar, *The Journal of Physical Chemistry C*, 2019, **123**, 8560-8568.

38. F. Sadeghi, B. Pashaei, B. N. Bideh, N. Sabahi, H. Shahroosvand and M. K. J. E. A. Nazeeruddin, *Energy Advances*, 2023, **2**, 1693-1701.

39. Y. Tan, H. Cheng, Y. Zhao, L. Wan and Z.-S. Wang, *Journal of Materials Chemistry A*, 2022, **10**, 7173-7185.

40. M. Azam, T. Du, Z. Wan, H. Zhao, H. Zeng, R. Wei, C. J. Brabec, J. Luo and C. Jia, *Energy & Environmental Science*, 2024, **17**, 6974-7016.

41. X. Ji, T. Zhou, X. Ke, W. Wang, S. Wu, M. Zhang, D. Lu, X. Zhang and Y. Liu, *Journal of Materials Chemistry A*, 2020, **8**, 5163-5170.

42. D. Wei, T. Wang, J. Ji, M. Li, P. Cui, Y. Li, G. Li, J. M. Mbengue and D. Song, *Journal of Materials Chemistry A*, 2016, **4**, 1991-1998.

43. T. Shimanouchi, H. Matsuura, Y. Ogawa and I. Harada, *Journal of physical and chemical reference data*, 1978, **7**, 1323-1444.

44. S. Majidi-Nezhad, N. Sabahi, H. Shahroosvand, N. Y. Nia and A. J. E. A. Di Carlo, *Energy Advances*, 2023, **2**, 1521-1530.

View Article Online
DOI: 10.1039/D5TA02440D

45. H. Choi, S. Park, S. Paek, P. Ekanayake, M. K. Nazeeruddin and J. J. J. o. M. C. A. Ko, *Journal of Materials Chemistry A*, 2014, **2**, 19136-19140.

46. M. Hosseini, D. E. Vanpoucke, P. Giannozzi, M. Berahman and N. J. R. a. Hadipour, *RSC advances*, 2020, **10**, 4786-4794.

47. Q. Fu, Z. Xu, X. Tang, T. Liu, X. Dong, X. Zhang, N. Zheng, Z. Xie and Y. J. A. E. L. Liu, *ACS Energy Letters*, 2021, **6**, 1521-1532.

48. C. H. Kuan, S. N. Afraj, Y. L. Huang, A. Velusamy, C. L. Liu, T. Y. Su, X. Jiang, J. M. Lin, M. C. Chen and E. W. G. J. A. C. Diau, *Angewandte Chemie*, 2024, e202407228.

49. L. Schein and A. J. P. R. B. McGhie, *Physical Review B*, 1979, **20**, 1631.

50. W.-J. Chi, Q.-S. Li and Z.-S. J. N. Li, *Nanoscale*, 2016, **8**, 6146-6154.

51. W.-J. Chi, P.-P. Sun and Z.-S. J. N. Li, *Nanoscale*, 2016, **8**, 17752-17756.

52. H. Ashassi-Sorkhabi and P. J. S. E. Salehi-Abar, *Solar Energy*, 2018, **173**, 132-138.

53. J. Wang, X. Wu, Y. Liu, T. Qin, K. Zhang, N. Li, J. Zhao, R. Ye, Z. Fan and Z. J. A. E. M. Chi, *Advanced Energy Materials*, 2021, **11**, 2100967.

54. H. Si, S. Zhang, S. Ma, Z. Xiong, A. Kausar, Q. Liao, Z. Zhang, A. Sattar, Z. Kang and Y. J. A. E. M. Zhang, *Advanced Energy Materials*, 2020, **10**, 1903922.

55. S. Jalili and A. J. C. M. S. Pakzadiyan, *Computational Materials Science*, 2023, **224**, 112161.

56. G. Kresse and J. J. P. r. B. Furthmüller, *Physical review B*, 1996, **54**, 11169.

57. X. Lai, F. Meng, Q. Q. Zhang, K. Wang, G. Li, Y. Wen, H. Ma, W. Li, X. Li and A. K. K. J. S. R. Kyaw, *Solar RRL*, 2019, **3**, 1900011.

58. D. Bharath, M. Sasikumar, N. R. Chereddy, J. R. Vaidya and S. J. S. E. Pola, *Solar Energy*, 2018, **174**, 130-138.

59. J. Xia, M. Sohail and M. K. J. A. M. Nazeeruddin, *Advanced Materials*, 2023, **35**, 2211324.

60. L. Hajikhanmirzaei, H. Shahroosvand, B. Pashaei, G. Delle Monache, M. K. Nazeeruddin and M. J. J. o. M. C. C. Pilkington, *Journal of Materials Chemistry C*, 2020, **8**, 6221-6227.

61. Z. Shen, Q. Han, X. Luo, Y. Shen, Y. Wang, Y. Yuan, Y. Zhang, Y. Yang and L. J. N. P. Han, *Nature Photonics*, 2024, 1-8.

62. A. Sun, C. Tian, R. Zhuang, C. Chen, Y. Zheng, X. Wu, C. Tang, Y. Liu, Z. Li and B. Ouyang, *Advanced Energy Materials*, 2024, **14**, 2303941.

View Article Online
DOI: 10.1039/D5TA02440D

63. A. Abudulimu, R. Sandoval-Torrientes, I. Zimmermann, J. Santos, M. K. Nazeeruddin and N. Martín, *Journal of Materials Chemistry A*, 2020, **8**, 1386-1393.

64. X. Sun, F. Wang, G. Yang, X. Ding, J. Lv, Y. Sun, T. Wang, C. Gao, G. Zhang and W. Liu, *Energy & Environmental Science*, 2025.

65. A. Dualeh, T. Moehl, N. Tétreault, J. Teuscher, P. Gao, M. K. Nazeeruddin and M. J. A. n. Grätzel, *ACS nano*, 2014, **8**, 362-373.

66. H.-S. Kim, I. Mora-Sero, V. Gonzalez-Pedro, F. Fabregat-Santiago, E. J. Juarez-Perez, N.-G. Park and J. J. N. c. Bisquert, *Nature communications*, 2013, **4**, 2242.

67. Q. Liao, Y. Wang, Z. Zhang, K. Yang, Y. Shi, K. Feng, B. Li, J. Huang, P. Gao and X. J. J. o. E. C. Guo, *Journal of Energy Chemistry*, 2022, **68**, 87-95.

68. K. Yang, Q. Liao, J. Huang, Z. Zhang, M. Su, Z. Chen, Z. Wu, D. Wang, Z. Lai and H. Y. J. A. C. I. E. Woo, *Angewandte Chemie International Edition*, 2022, **61**, e202113749.

69. L. Duan, Y. Chen, J. Yuan, X. Zong, Z. Sun, Q. Wu, S. J. D. Xue and Pigments, *Dyes and Pigments*, 2020, **178**, 108334.

70. K. Rakstys, S. Paek, P. Gao, P. Gratia, T. Marszalek, G. Grancini, K. T. Cho, K. Genevicius, V. Jankauskas and W. J. J. o. M. C. A. Pisula, *Journal of Materials Chemistry A*, 2017, **5**, 7811-7815.

71. S. Zhang, R. Wu, C. Mu, Y. Wang, L. Han, Y. Wu and W.-H. J. A. M. L. Zhu, *ACS Materials Letters*, 2022, **4**, 1976-1983.

72. Q. Liao, Y. Wang, M. Hao, B. Li, K. Yang, X. Ji, Z. Wang, K. Wang, W. Chi, X. J. A. A. M. Guo and Interfaces, *ACS Applied Materials*, 2022, **14**, 43547-43557.

73. S. N. Afraj, C. H. Kuan, J. S. Lin, J. S. Ni, A. Velusamy, M. C. Chen and E. W. G. J. A. F. M. Diau, *Advanced Functional Materials*, 2023, **33**, 2213939.

74. I. Mesquita, L. Andrade and A. J. C. Mendes, *ChemSusChem*, 2019, **12**, 2186-2194.

75. Y. Fang, X. Wang, Q. Wang, J. Huang and T. J. p. s. s. Wu, *physica status solidi*, 2014, **211**, 2809-2816.

76. H. Zheng, G. Liu, C. Zhang, L. Zhu, A. Alsaedi, T. Hayat, X. Pan and S. J. S. E. Dai, *Solar Energy*, 2018, **159**, 914-919.

77. S. Akin, M. Bauer, R. Uchida, N. Arora, G. Jacopin, Y. Liu, D. Hertel, K. Meerholz, E. Mena-Osteritz and P. J. A. A. E. M. Bäuerle, *Applied Energy Materials*, 2020, **3**, 7456-7463.

78. M. Petrus, T. Bein, T. Dingemans and P. Docampo, *Journal of Materials Chemistry A*, 2015, **3**, 12159-12162.

79. B. Xu, D. Bi, Y. Hua, P. Liu, M. Cheng, M. Grätzel, L. Kloo, A. Hagfeldt and L. Sun, *Energy & Environmental Science*, 2016, **9**, 873-877.

80. M. Saliba, S. Orlandi, T. Matsui, S. Aghazada, M. Cavazzini, J.-P. Correa-Baena, P. Gao, R. Scopelliti, E. Mosconi and K.-H. Dahmen, *Nature energy*, 2016, **1**, 1-7.

81. T. P. Osedach, T. L. Andrew and V. Bulović, *Energy & Environmental Science*, 2013, **6**, 711-718.

82. B. Pashaei, H. Shahroosvand, M. Ameri, E. Mohajerani and M. K. J. J. o. M. C. A. Nazeeruddin, *Journal of Materials Chemistry A*, 2019, **7**, 21867-21873.

View Article Online
DOI: 10.1039/D5TA02440D

Data Availability

supporting data are included in the article's supplementary information.